Fast beam photodissociation of the CH_2NO_2 radical

D. R. Cyr,[a] D. J. Leahy, D. L. Osborn,[b] R. E. Continetti,[c] and D. M. Neumark[d]
Department of Chemistry, University of California, Berkeley, California 94720 and Chemical Sciences Division, Lawrence Berkeley Laboratory, Berkeley, California 94720

(Received 16 August 1993; accepted 23 August 1993)

The photodissociation of the nitromethyl radical, CH_2NO_2, has been studied using a fast beam photofragment translational spectrometer. In these experiments, a fast beam of mass selected, internally cold nitromethyl radicals is formed via negative ion photodetachment of $CH_2NO_2^-$ and subsequently dissociated. The recoiling photofragments are detected in coincidence using a microchannel plate detector equipped with a time- and position-sensing anode. Two dissociation product channels are observed at each of three dissociation wavelengths investigated in the range 240–270 nm and are identified as (I) $CH_2NO_2 \rightarrow CH_2NO + O$ and (II) $CH_2NO_2 \rightarrow H_2CO + NO$. In marked contrast to the ultraviolet photodissociation of CH_3NO_2, no evidence is found for simple C–N bond fission to give (III) $CH_2NO_2 \rightarrow CH_2 + NO_2$. Translational energy and angular distributions were obtained for the two observed channels. The translational energy distribution of channel (I) peaks at only 5–8 kcal/mol, while the distribution for channel (II) peaks at ~ 60 kcal/mol. The angular distributions for both channels are largely isotropic. The nature of the electronic excitation and dissociation dynamics are considered at length. The upper state in the electronic transition is assigned to the $1\,^2B_1$ state. Results of attempts to model various aspects of the dissociation dynamics as statistical processes on the ground state surface indicate this mechanism is very unlikely. Instead, both dissociation channels are believed to occur primarily on excited state surfaces, and mechanisms for these processes are proposed.

I. INTRODUCTION

The study of molecular photodissociation processes has developed into one of the most productive and valuable areas of chemical physics in recent years.[1] This body of work has led to a detailed understanding of both the spectroscopy and dynamics associated with the dissociative electronic states in a wide variety of molecules. Moreover, photodissociation experiments provide one of the most direct means of determining bond dissociation energies. However, the vast body of these investigations have been undertaken on stable molecules; only a handful of photodissociation experiments on reactive free radicals have been performed to date. For most radicals, the excited states in general and the dissociative states in particular are poorly characterized, and the bond dissociation energies are not known very accurately. Hence, these species present an inviting target for photodissociation experiments.

This situation provided the motivation for the development in our laboratory of a photodissociation experiment especially well suited for studies of free radicals, based on a novel form of photofragment translational spectroscopy. In the standard version of photofragment translational spectroscopy,[2] a molecular beam is photolyzed and one measures the kinetic energy and angular distribution of the resulting fragments by a variety of techniques.[3] Thus far, the primary challenge met in extending this method to reactive free radicals[4,5] has been the difficulties involved in generating a clean, well-characterized molecular beam of these species. Our experiment uses a different approach in order to eliminate this problem. We produce mass selected, neutral free radicals from photodetachment of a fast (6–8 keV) beam of the corresponding negative ions. The resulting radicals are then photodissociated and the photofragments are detected with high efficiency. We can map out the dissociative excited states of a given radical by determining how the photodissociation cross section varies with dissociation photon energy. Subsequently, we perform dynamics experiments at selected wavelengths, using a coincidence detection scheme to determine the masses, kinetic energy release (KER), and recoil angle with respect to the laser polarization for each pair of photofragments formed. From this, we obtain photofragment kinetic energy and angular distributions as well as the yield for each fragmentation channel. Previously, we have applied this method to diatomic and triatomic species.[6–9] In this paper, we report our first results for a polyatomic molecule, the nitromethyl radical CH_2NO_2.

The nitromethyl radical is thought to be a primary intermediate in the combustion of nitromethane CH_3NO_2 formed by simple hydrogen abstraction.[10,11] Past experimental work on CH_2NO_2 is fairly limited. Chachaty and co-workers[12,13] obtained electron-spin resonance (ESR) spectra of the nitromethyl radical following γ irradiation of nitromethane at 77 and 195 K. Matrix isolation work using isotopic substitution performed by Jacox[11,14] resulted in the identification of all but one of the 12 ground state vibrational frequencies by infrared absorption, and the subsequent determination of the planar, C_{2v} geometry of the ground state. Jacox also ascertained that the threshold for

[a]NSERC (Canada) 1967 Predoctoral Fellow.
[b]NDSEG Predoctoral Fellow.
[c]Permanent address: Department of Chemistry, University of California, San Diego, La Jolla, CA 92093.
[d]NSF Presidential Young Investigator and Camille and Henry Dreyfus Teacher–Scholar.

photodissociation lies between 280–300 nm. The photoproducts resulting from dissociation at 280 nm were determined to be H_2CO and NO. It was noted that these could be either the nascent fragments or the products from caged recombination of CH_2+NO_2 formed by C–N fission. More recently, Metz *et al.*[15] recorded the photoelectron spectrum of the nitromethyl anion ($CH_2NO_2^-$). They determined the electron affinity of CH_2NO_2 to be 2.475 ± 0.010 eV and located an excited electronic state (the $1\,^2A_2$ state) 1.591 eV above the $\tilde{X}\,^2B_1$ ground state. In addition, *ab initio* calculations were performed to assist in identifying the one remaining unknown ground-state vibrational frequency (for the torsional mode) from the experimental data. Other theoretical work on the nitromethyl radical includes two previous *ab initio* calculations completed at the single and multiconfigurational self-consistent field (MCSCF) levels by McKee,[16,17] which attempted to identify and characterize the lowest electronic states.

In contrast to the relatively few studies of CH_2NO_2, the photodissociation of the analogous closed shell species nitromethane has been thoroughly studied. Depending on the method of excitation, three major pathways can contribute to dissociation

$$CH_3NO_2 \rightarrow CH_3NO+O, \quad (1)$$

$$\rightarrow CH_3O+NO, \quad (2)$$

$$\rightarrow CH_3+NO_2. \quad (3)$$

The ultraviolet photodissociation of CH_3NO_2 in the wavelength range from 190 to 220 nm has been investigated in the gas phase,[18–21] and also in solution.[22] This is a $\pi^* \leftarrow \pi$ excitation and leads exclusively to C–N bond fission [Eq. (3)]. Butler[20] has proposed two pathways to these products. The primary pathway is adiabatic, involving crossing onto a $\sigma^* \leftarrow n$ surface of the same symmetry as the initially excited state and leading to the production of NO_2 in the $1\,^2B_2$ electronic state. At the highest energies in this range, a diabatic dissociation pathway becomes energetically allowed, producing NO_2 in the $2\,^2B_2$ electronic state. Schoen *et al.*[23] have reported picosecond photodissociation studies of nitromethane at wavelengths between 238 and 337 nm, again finding only C–N bond fission in this region. The amount of electronically excited NO_2 was shown to increase with increasing photon energy, as determined by the ratio of fluorescence yield to laser-induced fluorescence yield measurements on the photoproducts. In contrast, infrared multiphoton dissociation (IRMPD) studies by Wodtke *et al.*[24,25] determined that when dissociation occurs on the ground state surface, there is a competition between the C–N bond fission process and rearrangement to form methyl nitrite, followed by nitric oxide elimination, as illustrated by Eq. (2). Beijersbergen *et al.*[26] have recently published a study in which the dissociative charge transfer neutralization of the nitromethane radical cation is described. This technique results in the formation of neutrals with excitation energies centered at 5.9 eV (Na charge exchange) or 7.2 eV (Cs charge exchange). In their study, they determined the major channels to be N–O and C–N fission [Eqs. (1) and (3)], while nitric oxide elimination [Eq. (2)] was observed as a minor channel.

The work on the nitromethyl radical reported here was largely motivated by our interest in learning how its photodissociation dynamics might differ from nitromethane. The matrix results obtained by Jacox[11] are particularly intriguing in this regard. If the H_2CO+NO photoproducts observed by Jacox are indeed nascent fragments, this would indicate that the primary UV photochemistry of CH_2NO_2 involves NO elimination rather than C–N bond fission as in CH_3NO_2. The collision-free environment in our experiment makes it possible to clearly identify the primary photofragments.

In the following section details of the experiment are discussed, while results and analysis of the photodissociation of the nitromethyl radical are presented in Sec. III. We unambiguously identify and characterize the nascent photoproducts of the ultraviolet photodissociation of CH_2NO_2. In doing so, we identify the following two dissociation channels: (I) $CH_2NO_2 \rightarrow CH_2NO+O$ and (II) $CH_2NO_2 \rightarrow H_2CO+NO$. The dissociation process that involves simple C–N bond fission (III) $CH_2NO_2 \rightarrow CH_2+NO_2$, is not observed. For the two observed channels, the branching ratio (I)/(II) changes from 1.19 to 1.76 on varying the photodissociation wavelength from 270 to 240 nm. In addition, the translational energy distribution $P(E_T)$ and the recoil anisotropy parameter as a function of kinetic energy release $\beta(E_T)$ are determined for each channel. These data imply fundamental differences in the dissociation dynamics for the two observed channels, providing insight into the dissociative mechanism involved in each channel. In Sec. IV, we discuss the implications of these observations on the dissociation mechanisms for the various channels. We note that a preliminary account of this work has been published elsewhere.[27]

II. EXPERIMENTAL APPROACH

Due to their open shell nature, free radicals typically have positive electron affinities. Our experiment utilizes this property in order to generate a pure, well-characterized packet of free radicals via photodetachment of the corresponding mass-selected negative ion. As an added advantage, the high laboratory frame kinetic energy imparted to the radicals during their acceleration prior to detachment allows the efficient collection and detection of photofragments simply by striking the face of a microchannel plate (MCP) detector.

A schematic of the fast radical beam photodissociation spectrometer used in this work is shown in Fig. 1. Details concerning the design of the fast radical beam spectrometer and the photofragment detection scheme have been given previously,[6,8] but there are several aspects of the experiment particularly germane to the present study which require description.

The basic experiment is as follows:

$$CH_2NO_2^- \xrightarrow{h\nu_1} CH_2NO_2+e^- \xrightarrow{h\nu_2} \text{fragments}. \quad (4)$$

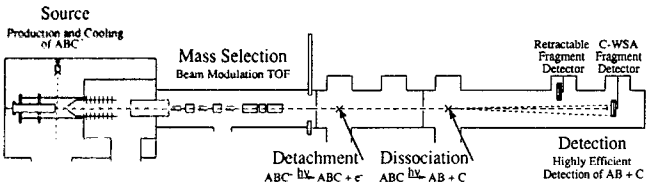

FIG. 1. A schematic illustration of the experimental apparatus. A more detailed diagram and explanation can be found in Refs. 6 and 8.

The nitromethyl anion $CH_2NO_2^-$ is prepared following the procedure of Metz *et al.*[15] using a pulsed molecular beam ion source similar to that developed by Lineberger and co-workers.[28] We first bubble a mixture of 10% NF_3 in N_2 through neat nitromethane (Eastman) at room temperature and 18 PSIG total pressure. A pulsed molecular beam valve operating at 60 Hz introduces this mixture to the source vacuum chamber. Immediately outside the nozzle orifice, the supersonic expansion is crossed with a continuous 1 keV electron beam. Low energy secondary electrons formed by electron impact ionization result in the production of F^- via dissociative attachment to NF_3. This fluorine anion abstracts a proton from nitromethane, forming $CH_2NO_2^-$, which undergoes cooling during the remainder of the expansion. Ions pass through a 3 mm diameter skimmer and are accelerated to 6 keV. They are then rereferenced to ground potential by the use of a potential "switch,"[29] and mass selected via a Bakker-type time-of-flight mass spectrometer.[30] After passing through a 1 mm beam-defining aperture, the anions are then photodetached using a tunable, pulsed, excimer-pumped-dye laser system, timed to intersect the mass of interest. Detachment laser pulse energies are 30–50 mJ/pulse and the laser is loosely focused with a 1 m focal length lens, 50 cm prior to intersecting the ion packet. Attenuation of the ion beam by the photodetachment light pulse can be as high as 50%.

The anions are vibrationally cold and the detachment wavelength is chosen to avoid the production of vibrationally excited radicals. We therefore photodetach the anions at a photon energy of 2.59 eV ($\lambda = 479$ nm), just above the electron affinity of CH_2NO_2, which was previously determined by anion photoelectron spectroscopy to be 2.475 eV.[15] This is low enough to avoid excitation of the ν_3 mode of the neutral, which is known from the photoelectron spectrum to be the primary active mode upon photodetachment.

Following detachment, all remaining negative ions are deflected out of the beam. The radicals must pass through a second 1 mm collimating aperture and are then intersected in the photodissociation region by the horizontally polarized, frequency-doubled output of a second pulsed excimer-pumped-dye laser, loosely focused by a 2 m lens. The photofragments are detected with one of two microchannel plate detectors lying 0.67 and 1.0 m downstream of the photodissociation region respectively; the closer detector is movable and is removed from the beam path when the more distant detector is in use. Photofragments typically have enough recoil kinetic energy to scatter out from the beam axis, thereby missing the blocking strips placed

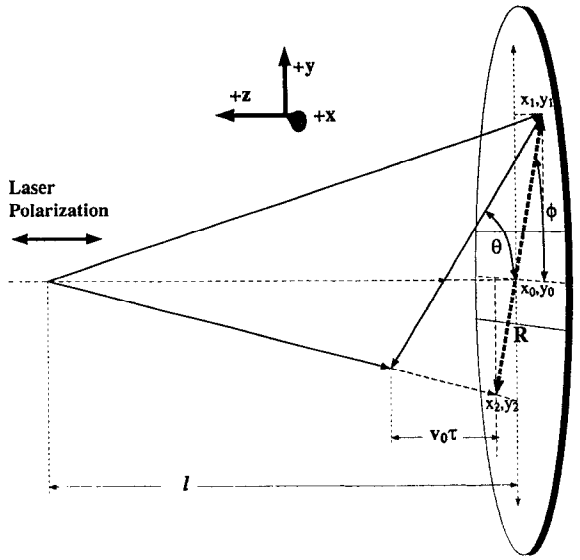

FIG. 2. A schematic of a typical dissociation event with the measured quantities necessary to calculation of fragment mass ratio KER and recoil angle with respect to laser polarization labeled.

across the center of the detectors (3 or 8 mm wide, respectively) to prevent undissociated radicals from impinging on the active area. The laboratory kinetic energies of the photofragments are generally >1 keV, ensuring a high ($\sim 50\%$) detection efficiency for those that strike the active area. The detector at 0.67 m is used for photodissociation cross section measurements; the total photofragment yield is monitored as the dissociation laser wavelength is varied. In general, this yields an approximate mapping of the dissociative electronic states of a given radical.

The photodissociation dynamics experiments are done using a more complex photofragment coincidence detection scheme. The laser is tuned to a wavelength at which photodissociation occurs and the photofragments are detected with the second detector 1 m from the photodissociation region. This detector is a two-particle time- and position-sensitive detector, similar in principle to the detector first developed by de Bruijn and Los,[31] although we use a coincidence wedge and strip anode (C-WSA)[8,32,33] rather than capacitive charge division for the position sensing. As illustrated in Fig. 2, for each photodissociation event, we measure the position of both fragments at the detector denoted (x_1, y_1) and (x_2, y_2), as well as the time delay between their arrival τ. This enables us to determine the photofragment masses, kinetic energy release, and scattering angle with respect to the dissociation laser polarization direction for each event. Because this is a coincidence measurement, we can process at most one event per laser pulse; ion densities in this experiment are sufficiently low so that this was not a problem. By summing over large numbers of dissociation events (2×10^4–8×10^4), we have obtained branching ratios as well as kinetic energy and angular distributions for each channel observed in this experiment.

The mass ratio of the two fragments is found by first

determining $r_i = \sqrt{(x_i-x_0)^2+(y_i-y_0)^2}$, the displacement of each fragment from the location of the radical beam center (x_0,y_0) on the detector face. The mass ratio of the two fragments is then given approximately by the inverse of the ratio of these displacements

$$\frac{m_1}{m_2}=\frac{r_2}{r_1}\{1-[(v_0\tau)/l]\}\cong\frac{r_2}{r_1}. \tag{5}$$

Once the fragment masses are determined, Eqs. (6) and (7), originally derived by De Bruijn and Los,[31] are used to obtain the center-of-mass kinetic energy release (KER) and fragment recoil angle θ, measured with respect to the polarization vector of the laser, for each dissociation event

$$\theta=\tan^{-1}\left(\frac{R}{v_0\tau}\right), \tag{6}$$

$$\mathrm{KER}=E_0\cdot\left(\frac{m_1m_2}{M^2}\right)\cdot\frac{[(v_0\tau)^2+R^2]}{l^2}\cdot\left(1+2\frac{m_2-m_1}{M}\frac{v_0\tau}{l}\right). \tag{7}$$

Here $R = \sqrt{(x_2-x_1)^2+(y_2-y_1)^2}$ is the relative separation of the two fragments, M is the parent radical mass, m_1 and m_2 are the fragment masses striking the upper and lower halves of the detector, respectively, l is the flight length, and E_0 and v_0 are the primary beam energy and velocity, respectively. τ is taken to be positive if the upper fragment strikes the detector first.

In Eq. (5), the chief source of uncertainty is the dependence of r_1 and r_2 on an explicit knowledge of (x_0, y_0), the detector coordinates where the center of mass of the dissociating system would be found (i.e., where the parent radical, if it had not dissociated, would strike the detector). The radical beam is about 1 mm full width at half-maximum (FWHM) in diameter, resulting in a fragment mass resolution $(m/\Delta m)$ of about 15 for the results reported here. In contrast, Eqs. (6) and (7) do not require an explicit knowledge of (x_0, y_0) and therefore the center-of-mass uncertainty does not contribute to the energy and scattering angle, assuming the product masses can be identified unambiguously. The measured spatial resolution is on the order of 75 μm full width at half maximum in y and 130 μm in x, while timing resolution is about 0.5 ns. Energy resolution as high as 10 meV has been demonstrated during calibrations using the predissociation of O_2 through the Schumann-Runge band,[9] but is approximately 30 meV (0.69 kcal/mol, 240 cm^{-1}) in these studies.

Upon the completion of a photodissociation dynamics experiment, we first separate the data into different mass channels following Eq. (5). For each channel, we then construct a two-dimensional array in E_T and theta into which each coincident dissociation event is binned. The product channel specific energy-angle arrays, denoted here as $\mathscr{S}(E_T,\theta)$, are determined using Eqs. (6) and (7). From this, we obtain the true joint energy and angular distribution $\mathscr{P}(E_T,\theta)$ for each channel by dividing by the "detector acceptance function" $\mathscr{D}(E_T,\theta)$

$$\mathscr{P}(E_T,\theta)=\mathscr{S}(E_T,\theta)/\mathscr{D}(E_T,\theta). \tag{8}$$

The detector acceptance function accounts for the finite acceptance of the detector as a function of E_T and theta. For example, fragments with lower recoil energies and/or values of theta close to 0° or 180° may not strike the detector because of the beam block, while some high energy fragments at values of theta close to 90° miss the detector because of its finite size. The straightforward numerical determination of $\mathscr{D}(E_T,\theta)$ is discussed in Ref. 8.

As mentioned above, the dual-wedge-and-strip anode requires an 8 mm wide horizontal blocking strip which shields the microchannel plates over a small region above the interface of the two anodes to prevent the undissociated radical beam from impinging on the detector face. However, it also prevents photofragments with very low center-of-mass kinetic energy from being detected. This effect is magnified in the case of fragments with unequal masses. The heavy fragment scatters out of the beam more slowly than the light and is more likely to be blocked, but both fragments must be detected to be recorded as a coincidence event. In order to improve coincidence detection of low energy, unequal mass fragments, the detector can be positioned slightly off center vertically with respect to the radical beam axis. In the experiments reported here, such a product channel was identified early on, and the data were then collected with the center of the detector 1.9 mm lower than the radical beam axis. This enables heavy fragments that would have otherwise struck the blocking strip to clear the top edge. Because the correlated light fragments have a greater recoil velocity due to momentum conservation, they are able to travel the correspondingly larger distance necessary to clear the bottom of the blocking strip. The effect of this offset on the detector acceptance function is included in the analysis of the data.

III. RESULTS AND ANALYSIS

Photodissociation cross section measurements of the CH_2NO_2 radical were taken across the wavelength range from 240 to 270 nm. The photodissociation cross section scans appeared to be structureless, with the cross section peaking near 240 nm and decreasing monotonically by about a factor of 5 at 270 nm. Most of the photodissociation dynamics data were taken at 240 nm, corresponding to a photon energy of 119.1 kcal/mol, where the dissociation signal was most intense. Supplementary data were recorded using longer wavelengths of 255 and 270 nm, corresponding to photon energies of 112.1 and 105.9 kcal/mol, respectively.

A. Identification of photodissociation channels

Prior to any further analysis, it is necessary to determine which fragmentation channels occur in the photodissociation of CH_2NO_2. Many channels are energetically allowed in the present case of CH_2NO_2, a six atom radical to which ~5 eV excitation energy is imparted. Even if only one dissociation channel is active, the analysis of time and position data to obtain translational energy distributions depends on first identifying the masses of the photofrag-

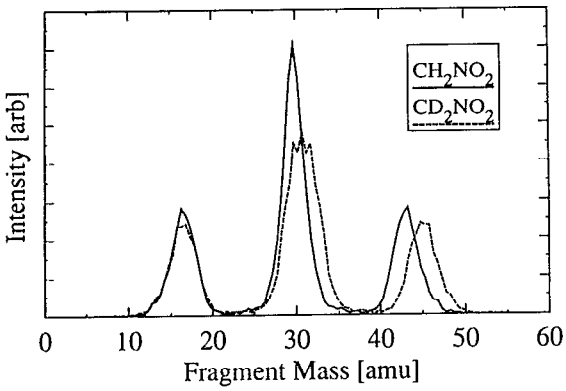

FIG. 3. Photofragment mass spectrum from the 240 nm dissociation of the nitromethyl radical (CH_2NO_2; solid line) and the d_2-nitromethyl radical (CD_2NO_2; dashed line). Areas under the mass peaks do not accurately reflect the mass channel branching ratio because they are uncorrected for detector acceptance (see the text).

ments produced. The presence of two or more active dissociation channels demands the ability to determine which channel *each* dissociation event corresponds to.

The photofragment mass spectrum for CH_2NO_2 at 240 nm is shown in Fig. 3. Note that this plot is constructed from the data by determining the photofragment mass ratio in each event, and thus the fraction of the total mass M ($=60$ amu) of the parent radical for each fragment, resulting in a mirror image about $M/2$. The mass spectrum indicates the presence of two dissociation channels. Although the mass resolution is limited, it appears that in one channel, the fragment masses are 16 and 44 amu, while in the other, both fragments have mass 30 amu. This would indicate that the two dissociation channels are (I) CH_2NO+O and (II) H_2CO+NO.

In order to verify these assignments, the photofragment mass spectrum of CD_2NO_2 was also obtained at 240 nm, and the results are superimposed on the CH_2NO_2 mass spectrum in Fig. 3. The differences in the two spectra upon deuteration are the following: the mass peak centered at 16 amu remains fixed while the mass peak at 44 amu shifts to 46 amu, and the mass peak centered at 30 amu broadens towards higher mass and appears to be centered at 31 amu. The first difference shows that the photofragments with mass ratio close to 3:1 indeed corresponds to (I) $CH_2NO_2 \rightarrow CH_2NO+O$, since there can be no H/D atoms in the lighter mass fragment. Although the mass fragments from channel (III) $CH_2NO_2 \rightarrow CH_2+NO_2$ (14 and 46 amu) are similar to those of channel (I), upon isotopic substitution the lower mass peak would shift from 14 to 16 amu, while the heavier mass fragment would remain fixed at 46 amu. We therefore estimate an upper limit for the presence of channel (III) products of 4%. The second observed difference confirms the presence of channel (II), $CH_2NO_2 \rightarrow H_2CO+NO$, since the dissociation products from CH_2NO_2 should both have a mass of 30 amu, while the deuterated analog CD_2NO_2 should have dissociation products with masses of 32 and 30 amu, respectively. The deuterated mass spectrum eliminates another energetically feasible channel with comparable masses corresponding to O_2 elimination, $CH_2NO_2 \rightarrow H_2CN+O_2$. The fragment masses of this excluded channel would change from 28:32 to 30:32 upon deuteration, resulting in an expected narrowing of the central peak of the mass spectrum, contrary to our observation. This channel is assigned a similar estimated upper limit of 4%.

While the mass spectra we have obtained do not show evidence for the presence of any dissociation channels other than the two identified above, we are unable to comment on channels involving extreme mass ratios because of the unfavorable kinematics involved. When two fragments have very disparate masses, as in the case of hydrogen bond fission, either the light fragment will recoil outside the maximum radius of the detector, or the heavy fragment will fail to clear the blocking strip, or both, depending on the recoil energy and angle of the event. Therefore, a conceivable channel that would go undetected in our experiment involves loss of a H atom, forming $HCNO_2+H$. Although there is no literature value for the C–H bond energy of nitromethyl radical, we expect it to be close to the 100 kcal/mol value found in the C–H bond in CH_3NO_2,[15,34] largely unaffected by the open shell nature of the radical. This is quite high compared to the available energy in these experiments and the energies of the channels which are known to be occurring (see below), so it is doubtful that this channel is active.

B. Kinetic energy release and angular distributions

Once the photodissociation channels are identified, we can determine the center-of-mass kinetic energy and angular distributions for each channel. The energy and angular distribution $\mathscr{P}(E_T,\theta)$ for a one-photon dissociation can be expressed as

$$\mathscr{P}(E_T,\theta)=P(E_T)[1+\beta(E_T)P_2(\cos\theta)], \tag{9}$$

where θ is the angle between the photofragment recoil vector and the electric vector of the dissociation laser, $P_2(\cos\theta)$ is the second Legendre polynomial, $\beta(E_T)$ is the anisotropy parameter as a function of translational (or kinetic) energy, and $P(E_T)$ is the angle-integrated translational energy distribution. The anisotropy parameter β can range from $\beta=+2$ to $\beta=-1$, corresponding to a $\cos^2\theta$ distribution and a $\sin^2\theta$ distribution of recoil vectors, respectively.[35]

$\mathscr{P}(E_T,\theta)$ is derived from the data as described in Sec. II. The photofragment anisotropy parameter $\beta(E_T)_i$ is found for each kinetic energy interval $(E_i-\Delta E/2,\ E_i+\Delta E/2)$ by performing a least-squares fit to Eq. (9). The ΔE intervals chosen for this procedure were 4.6 kcal/mol for channel (I) and 9.2 kcal/mol for channel (II). Only when the data becomes very sparse (i.e., in the "tail" of the KER distribution near the energetic limit for a given channel) do we find that this method of analysis breaks down. In these restricted regions containing very little data, we cannot determine $\beta(E_T)$ and it is assumed to be zero (implying an isotropic recoil angular distribution). The final step in this direct inversion analysis is to find the angle-

TABLE I. Some possible product channels for the ultraviolet photodissociation of the nitromethyl radical. On the right, the energies available to the products following dissociation at the three wavelengths used in this work are listed. Heats of formation for CH_2NO_2 and CH_2NO are taken from Metz *et al.* (Ref. 15) and Melius (Ref. 36) respectively, while all other thermochemical information is obtained from Ref. 34. Channels (I) and (II) were observed as major channels in these experiments, while channel (III), corresponding to C–N bond fission, was found to be absent.

Product channel	Masses (amu)	D_0 (kcal/mol)	$h\nu - D_0$ (kcal/mol) 240 nm	255 nm	270 nm
(I) CH_2NO+O	44+16	72±6	47	40	34
(II) H_2CO+NO	30+30	−33.7±3	152.8	145.8	139.6
(III) CH_2+NO_2	14+46	71.2±3	47.9	40.9	34.7

integrated translational energy distribution $P(E_T)$ at the highest energy resolution. Using the appropriate $\beta(E_T)$ as determined above, we determine $P(E_T)$ for energy intervals of 0.575 kcal/mol in channel (I) and 1.150 kcal/mol in channel (II). These intervals are comparable to the instrumental resolution.

Table I shows the energies relative to the nitromethyl of the two observed product channels in addition to the absent C–N bond fission channel. The heat of formation of CH_2NO_2 is taken to be 30.4±3 kcal/mol,[15] while the heat of formation for CH_2NO has been calculated by Melius[36] to be 43±6 kcal/mol. All other thermochemical data are relatively well known and are obtained from Ref. 34.

Figure 4 shows the $P(E_T)$ distribution of channel (I) $CH_2NO_2 \rightarrow CH_2NO+O$ at the three wavelengths used in this study 240, 255 and 270 nm. All three of these distributions are peaked close to zero KER, with the 240 nm distribution peaking furthest away at 5–8 kcal/mol. The $P(E_T)$ distributions obtained at the other wavelengths peak closer to zero, but larger statistical uncertainties make the exact determination of their maxima difficult. For this channel the lowest observable KER, because of the presence of the blocker, is 2.0 kcal/mol. The observed mean KERs are 11.4, 11.0, and 10.8 kcal/mol for 240, 255, and 270 nm photodissociation, respectively. These values are upper bounds for the true mean KER because of the unobserved fragments with a KER of less than 2.0 kcal/mol. Barring the presence of an excursion in the $P(E_T)$ distribution below 2.0 kcal/mol, the overestimate in the mean KERs listed above is less than 10%. The maximum kinetic energy release in the 240 nm data, for which the statistical error bars are smallest, is 44±1 kcal/mol. This observation, combined with the well-known $\Delta_f H^0_{(0\,K)}$ of an O atom (59.0 kcal/mol) (Ref. 34) and the $\Delta_f H^0_{(0\,K)}$ for CH_2NO_2 given by Metz *et al.*[15] places an upper bound on the $\Delta_f H^0_{(0\,K)}$ for CH_2NO of 47±3 kcal/mol. This upper bound is very close to the $\Delta_f H^0_{(0\,K)}$ for CH_2NO of 43±6 kcal/mol given by Melius.[36] It is well below the upper bound of $\Delta_f H^0_{(0\,K)}$ (CH_2NO) = 99 kcal/mol given by Beijersbergen *et al.*;[26] however, in their calculations, they use the most probable kinetic energy release rather than the maximum observed kinetic energy release. This, coupled with their assumption that all excess energy is measured as kinetic energy, results in a very conservative upper bound.

Figure 5 shows the $P(E_T)$ of channel (II), $CH_2NO_2 \rightarrow H_2CO+NO$, for 240, 255, and 270 nm photolysis. All three energy distributions have a broad peak near 55 kcal/mol, with a mean KER of 58 kcal/mol. High en-

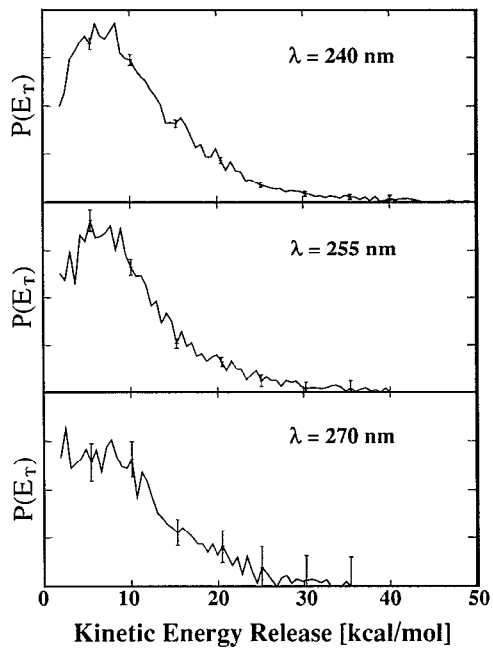

FIG. 4. $P(E_T)$ distribution plots for the CH_2NO+O photodissociation channel taken at the three labeled wavelengths. Error bars represent 1σ uncertainty.

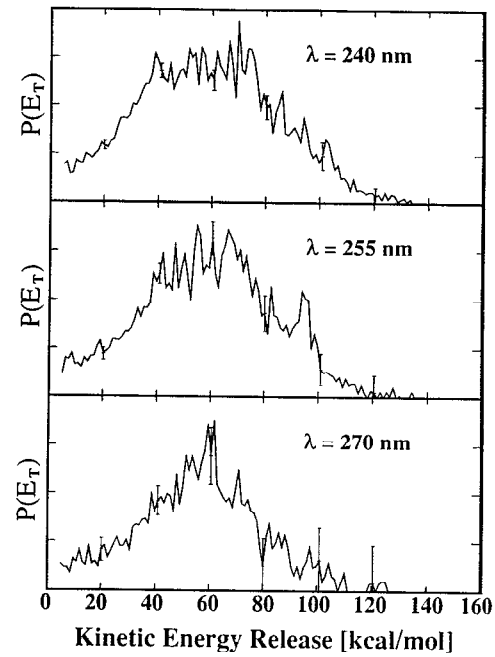

FIG. 5. $P(E_T)$ distribution plots for the H_2CO+NO photodissociation channel taken at the three labeled wavelengths. Error bars represent 1σ uncertainty.

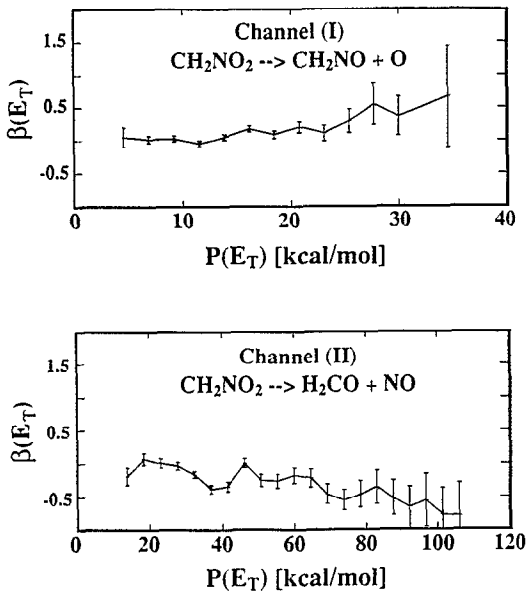

FIG. 6. Recoil anisotropy factor β determined from the data as a function of recoil energy E_T for both channel (I) (CH_2NO+O) and channel (II) (H_2CO+NO) at 240 nm.

ergy tails in the $P(E_T)$ plots extend up to about 20 kcal/mol below the energetic limit of this channel, which is 153 kcal/mol at 240 nm. Upon changing photon energies, the mean KER changes very little; the major effect instead is that the higher wavelength $P(E_T)$ distributions are narrower, being more strongly peaked near the mean KER.

Figure 6 is a plot of the fragment recoil anisotropy parameter β as a function of recoil energy for channels (I) and (II) as determined from the 240 nm data. β for channel (I) appears to be essentially zero until the upper limit of observed KERs where the uncertainty associated with the measured values of β includes zero in all but one case. β for channel (II) is also found to be quite close to zero at low values of KER. Both of these plots are representative of the dependence of β on KER at all three wavelengths for the respective channels; within the experimental uncertainty, the $\beta(E)$ plots did not appear to depend on the photon energy. We note that nearly isotropic angular distributions were also seen in the 193 nm photodissociation of nitromethane.[18]

Channel (II) may also involve the secondary dissociation of the most highly internally excited portion of the H_2CO formed. The exothermicity of channel (II) is 34 kcal/mol, so that at 240 nm (119.1 kcal/mol), fully 153 kcal/mol of energy is available for distribution among the products' degrees of freedom. This energy is well above the 80 kcal/mol barrier to dissociation to H_2+CO. Of course, Fig. 5 shows that much of the available energy appears as product translation. In addition, the NO bond order changes from 1.5 to 2.5 during elimination, which is likely to result in vibrationally excited NO, further decreasing the energy available for partitioning into H_2CO internal degrees of freedom. Nonetheless, some fraction of H_2CO might be expected to possess sufficient internal energy to undergo secondary dissociation on the nanosecond time scale. A second dissociation pathway for H_2CO, forming $H(^2S)+HCO\ \tilde{X}$ with very little KER is expected to dominate the decomposition of H_2CO much above its threshold of 96 kcal/mol.[37] In both cases, however, the kinematics are such that the velocity of the heavy fragment (CO or HCO) will be very close to that of the original H_2CO photofragment, whereas the light fragment will fly out of the beam and miss the detector. The net result, at worst, will be a slight blurring of the translational energy distribution for channel (II). Even in the absence of secondary dissociation, one would not expect to resolve any structure in the translational energy distribution for channel (II) since two molecular fragments are produced. Hence, the effects of secondary dissociation on the overall appearance of the distribution should be very small.

C. Branching ratios

Branching ratios are easily determined from the foregoing KER analysis by summing the area under the KER curves to obtain the total population of each channel at each wavelength. As can be seen from Table II, the branching ratio is near unity at the lowest photon energy, but definitely favors channel (I), involving O atom loss, as the photon energy is increased. The uncertainties given with these numbers derive chiefly from two sources — statistical error and uncertainty in $\beta(E_T)$. Statistical error in each channel is well modeled by counting statistics. The second source of uncertainty is due primarily to the absence of knowledge of $\beta(E_T)$ for the small amount of data found at energies where the $P(E_T)$ is very low. By assuming values of $\beta(E_T)$ that represent the possible extremes in these regions, and the limits of uncertainty in the regions where $\beta(E_T)$ is well determined, we estimate the uncertainty in branching ratio from this source.

TABLE II. This table is a compilation of the observed $P(E_T)$ data for both channels at the three wavelengths (photon energies) used in our experiments. The average kinetic energy release for each channel and the branching ratio measurements {expressed as the quotient [channel (I)/channel (II)]} are given.

Wavelength (nm)	Photon energy (kcal/mol)	Channel (I) CH_2NO+O ⟨KER⟩ (kcal/mol)	Channel (II) H_2CO+NO ⟨KER⟩ (kcal/mol)	Branching ratio [channel (I)/channel (II)]
270	105.9	11.4	59	1.19(+0.37, −0.21)
255	112.1	11.0	59	1.29(+0.25, −0.16)
240	119.1	10.8	56	1.76(+0.27, −0.16)

IV. DISCUSSION

In the following discussion, we compare our results for the photodissociation of the nitromethyl radical to the known photodissociation behavior of nitromethane. We then identify the initial electronic transition used in the excitation of CH_2NO_2 in the present experiment. Subsequently, we develop the argument that the observed product branching ratios (particularly the absence of C–N bond fission), combined with the translational energy distribution for channel (II), imply that dissociation is not occurring via a statistical process on the ground state CH_2NO_2 surface. Rather, NO elimination most likely results from nuclear dynamics on an excited state surface, aided by the coordinative unsaturation of the C atom in the nitromethyl radical. We will also argue that the other observed channel, involving N–O bond fission, must similarly be occurring along an excited pathway, and we identify a plausible mechanism.

A. Comparison to nitromethane

The identities of the product channels we observe in the ultraviolet photodissociation of the nitromethyl radical represent a significant departure from what one might expect based on the known UV photofragmentation behavior of the closest closed-shell analog nitromethane. Nitromethane exclusively undergoes C–N bond fission following UV absorption,[18–23] whereas the analogous channel (III) is absent in CH_2NO_2 photodissociation. Instead, we have identified two major channels — channel (I) N–O bond fission and channel (II) the elimination of NO. Primary N–O bond fission has not been observed in any collision-free nitromethane photodissociation experiments, although it has been observed in the nitromethane radical cation dissociative charge neutralization experiments of Beijersbergen *et al.*[26] They also reported a minor channel identified as $H_2CO+NOH$ (or HNO). Only in infrared multiphoton dissociation (IRMPD) studies[24,25] has the analogous CH_3O+NO photodissociation product channel been seen for nitromethane.

Some of the differences between CH_2NO_2 and CH_3NO_2 can be understood in terms of the relevant bond dissociation energies. As shown in Table I, the N–O and C–N bond strengths are roughly comparable in CH_2NO_2 ($\approx$71 kcal/mol). In contrast, the bond dissociation energies for the N–O and C–N bonds in CH_3NO_2 are 95 and 60.6 kcal/mol, respectively.[34] The slightly stronger C–N bond in CH_2NO_2 presumably arises from the C–N π bonding interaction via the half-filled $2b_1$ molecular orbital. The N–O bond is considerably stronger in CH_3NO_2 than in CH_2NO_2 or other related radicals: e.g., the N–O bond dissociation energies of NO_2 and NO_3 are 72.7 and 49.2 kcal/mol, respectively.[34,5] While the absence of N–O fission in the UV photodissociation of nitromethane is perhaps not so surprising in light of the bond strengths, the preference of N–O over C–N bond fission in CH_2NO_2 photodissociation is an intriguing bond selective effect worthy of further consideration.

The observation of NO elimination in the UV photodissociation of CH_2NO_2 but not CH_3NO_2 is also of interest. As mentioned above, CH_3O+NO products have been seen in the infrared multiphoton dissociation of nitromethane;[25] these are produced in competition with the products of C–N bond fission with a branching ratio of $(CH_3O+NO)/(CH_3+NO_2)\approx 0.6$. In these studies, the mechanism proposed for CH_3O+NO formation was isomerization to methyl nitrite (CH_3ONO) over a barrier involving a three-center C–N–O transition state followed by CH_3O–NO bond fission, all on the ground state electronic surface of the system. Using a statistical model for the competition between isomerization and C–N bond fission, the isomerization barrier height was estimated to be 55.5 kcal/mol. Saxon and Yoshimine[38] later performed calculations to more fully characterize this nitro-nitrite isomerization transition state and determined that the C–N and C–O bond lengths are 3.4 and 3.65 Å, respectively. These bond lengths are very large compared with the CH_3NO_2 ground state C–N equilibrium bond distance of 1.489 Å,[39] resulting in a transition state whose energy is calculated to be 56.7 kcal/mol, only 0.4 kcal/mol less than their calculated C–N bond dissociation energy. The very unfavorable geometry of the rearrangement transition state and accompanying high barrier is a consequence of the inability of the fully saturated C atom in nitromethane to form a new bond without first breaking an existing bond. In the case of NO elimination from CH_2NO_2, one also expects to pass through some type of C–N–O transition state, but the formation of such a structure should be facilitated because the C atom in CH_2NO_2 is coordinatively unsaturated. This effect should not be limited to the ground state surface.

The dynamics involved in the NO elimination channel that we observe are also quite different from the above mentioned IRMPD study of CH_3NO_2. In the IRMPD experiment, the translational energy distribution for NO elimination peaked at zero kinetic energy. This is the characteristic distribution for a statistical bond fission in the absence of a barrier in the reverse direction and indicates that the CH_3ONO well is sufficiently deep for "rerandomization" of the available energy to occur after crossing the isomerization transition state. Indeed, the heat of formation of methylnitrite is virtually identical to that of nitromethane (only $\sim$2 kcal/mol higher), resulting in methylnitrite being $\sim$40 kcal/mol stable with respect to CH_3O+NO products.[34] The situation in our experiment is quite different—the translational energy distribution for NO elimination peaks at high kinetic energy ($\sim$60 kcal/mol). This implies that, regardless of the details, little or no rerandomization occurs prior to dissociation to H_2CO+NO products.

B. Nature of the initially excited electronic state

In order to have any detailed understanding of the dissociation mechanisms operative in CH_2NO_2, we need to know which electronic transition is responsible for the absorption band probed in our experiment. CH_2NO_2 has a $^2B_1$ ground state with molecular orbital configuration $[\cdots(8a_1)^2(5b_2)^2(1a_2)^2(2b_1)]$. Figure 7 gives a qualitative

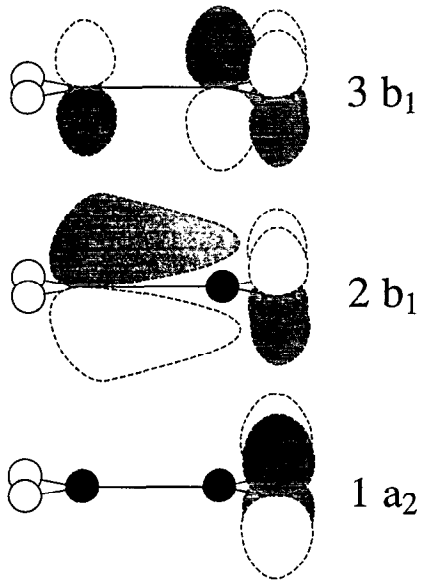

FIG. 7. A form of the $1a_2$, $2b_1$, and $3b_1$ molecular orbitals determined from *ab initio* calculations performed on $CH_2NO_2^-$.

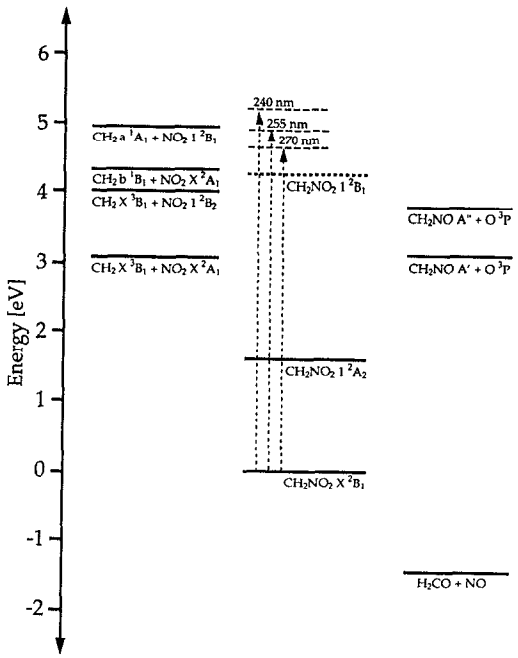

FIG. 8. Energetics of the nitromethyl radical and selected energetically allowed product channels (not all products shown are observed). States whose energies are known relatively well are represented by solid lines located at their origin, while a dashed line is used to denote the approximate location of the $1\,^2B_1$ state (see the text).

picture of the $1a_2$ and $2b_1$ molecular orbitals as well as the unoccupied $3b_1$ molecular orbital obtained by undertaking a minimal basis set [Slater-type orbital (STO-3G)] geometry optimization calculation using the GAUSSIAN 88 package[40] on $CH_2NO_2^-$. A low-lying excited state of CH_2NO_2, the $1\,^2A_2$ state, results from the $2b_1 \leftarrow 1a_2$ transition. This was the excited state observed in the $CH_2NO_2^-$ photoelectron spectrum,[15] formed by the removal of an electron from the $1a_2$ molecular orbital of the anion, and found to lie only 36.7 kcal/mol above the ground state. Figure 7 shows that the $2b_1 \leftarrow 1a_2$ transition involves excitation from a nonbonding N–O π orbital to a π orbital which is N–O antibonding and C–N bonding. However, because the $1\,^2A_2$ state lies so far below the photon energies used in our experiment (> 105 kcal/mol), it is an unlikely candidate for the initial excited state. The $2b_1 \leftarrow 5b_2$ transition yielding a $^2B_2$ excited state is not optically allowed in C_{2v} symmetry. Two other excited states resulting from $\pi^* \leftarrow \pi$ transitions are more attractive options—the $1\,^2B_1$ state, from the $3b_1 \leftarrow 2b_1$ transition, and the $2\,^2A_2$ state from the $3b_1 \leftarrow 1a_2$ transition. The $3b_1 \leftarrow 2b_1$ transition is analogous to the transitions seen around 230 nm for several alkanenitronate ($R'RC{=}NO_2^-$) anions in solution.[41] The $3b_1 \leftarrow 1a_2$ transition is more localized on the NO_2 group than the other two transitions and strongly resembles the $\pi^* \leftarrow \pi$ transition in nitromethane between 190–220 nm. This is the transition accessed in most nitromethane UV photodissociation experiments.[18–21]

The lowest energy transitions in solvated alkanenitronate anion spectra result in bands that peak near 230 nm and extend up to 250–260 nm.[41] This corresponds approximately with our photodissociation cross section measurements, although the band in the radical appears somewhat red shifted. The C–N bond distance in the anion ground state is considerably shorter than in the neutral (1.347 vs 1.430 Å, according to our previous *ab initio* calculations[15]), and the π^* orbital populated by this transition is C–N antibonding. One would expect the vertical transition energy to be lower in the radical than in the corresponding anion, so the observed red shift appears reasonable. Conversely, one might expect the $3b_1 \leftarrow 1a_2$ transition to occur at a higher energy in CH_2NO_2 than the $\pi^* \leftarrow \pi$ transition in nitromethane because the C–N π^* antibonding interaction in CH_2NO_2 is absent in nitromethane. Any blue shifting of this transition would place it well beyond the range of photodissociation wavelengths used in our experiments. Based on these considerations, we assign the $1\,^2B_1$ state resulting from the $3b_1 \leftarrow 2b_1$ transition as the initially prepared excited electronic state.

Figure 8 shows the energies of the CH_2NO_2 electronic states relative to the dissociation channels (I), (II), and (III). The location of the $1\,^2B_1$ state on this diagram is intended to indicate the lowest energy at which transitions from the ground state to the $1\,^2B_1$ state occur and is estimated according to the lowest energy at which electronic excitation of CH_2NO_2 leads to dissociation. According to the matrix isolation study of Jacox,[11] the dissociation threshold is known to be between the wavelengths of 300 nm (4.13 eV) and 280 nm (4.42 eV). We therefore place the $1\,^2B_1$ state (somewhat arbitrarily) at 4.25 eV. The energetics of low-lying electronic states of channels (I) and (III) are also shown; the excited states of CH_2 and NO_2 are reasonably well-characterized experimentally, while the locations of the ground and first excited states of CH_2NO are from a fourth-order Møller–Plesset (MP-4) BAC *ab initio* calculation by Melius.[36]

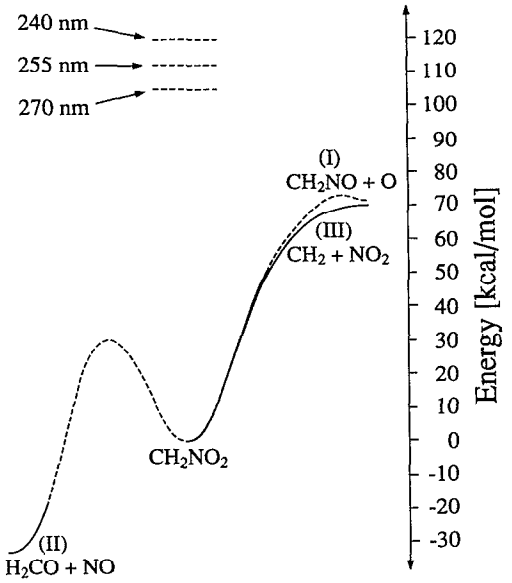

FIG. 9. A schematic of the adiabatic minimum energy pathways to all three product channels on the ground state surface of CH_2NO_2.

C. Dissociation mechanisms

Our assignment of the electronic transition accessed in these experiments offers an immediate if somewhat unspectacular reason for the different product channels seen in the CH_2NO_2 and CH_3NO_2 photodissociation experiments. In nitromethane dissociation, the π^* state accessed near 200 nm, which correlates diabatically to $CH_3 + NO_2(2\,^2B_2)$ products, is believed to be predissociated by a σ^* repulsive state of the same symmetry that correlates to lower energy $CH_3 + NO_2(1\,^2B_2)$ products. Since we believe we are exciting a qualitatively different transition in CH_2NO_2, involving a different excited state surface, this mechanism would not be operative. It remains to be understood how CH_2NO_2 does dissociate, and this will now be considered in detail.

1. The possible role of ground state statistical dissociation

To explain product branching ratios and translational energy distributions in a given photodissociation experiment, a simple model to consider is rapid internal conversion to the ground state potential energy surface. One should then be able to predict the product branching ratios by a statistical model such as the Rice–Ramsperger–Kassel–Marcus (RRKM) theory.[42,43] Such a statistical treatment was successfully used by Wodtke *et al.* to interpret the IRMPD of nitromethane.[25] Figure 9 shows a schematic of the potential energy along the reaction coordinates for channels (I)–(III) on the ground state surface of CH_2NO_2. We would expect "loose" transition states for the simple bond fission channels (I) and (III) and a "tight" transition state, presumably involving a three-membered C–N–O ring, for NO elimination channel (II).[44] The high kinetic energy release associated with channel (II) is consistent with passage over a barrier associated with the tight transition state, while the translational energy distribution for channel (I) peaks near zero, the expected "statistical distribution" for simple bond fission [perhaps over a small barrier in the reverse direction, consistent with the $P(E_T)$ distribution maximum at several kilocalories per mole]. However, ground state $CH_2 + NO_2$ correlates to the ground state of CH_2NO_2 both diabatically and adiabatically. This means there should be no barrier to the $CH_2 + NO_2$ recombination reaction, so the loose transition state associated with C–N bond fission will lie about 71 kcal/mol (i.e., the bond dissociation energy) above the CH_2NO_2 well. Since the N–O and C–N bond dissociation energies are very close, the transition state for channel (I) must also lie at least as high; it will be higher if there is a barrier along the reaction coordinate for channel (I). In addition, the preexponential A factor in the Arrhenius rate equation for the C–N bond fission channel will be larger since channel (III) yields two polyatomics, as opposed to a polyatomic plus an atom, and will thus have a greater gain in entropy on going from the reactant to the activated complex.[43] Thus, even with no barrier to N–O bond fission above the bond dissociation energy, we expect a statistical model to yield a greater rate of C–N bond fission than N–O bond fission. This is incompatible with the absence of C–N bond fission products observed in the present experiment and immediately indicates that the N–O bond fission channel cannot be explained by statistical dissociation on the ground state surface. We shall return to this channel subsequently.

While it appears certain that a statistical dissociation on the ground state surface cannot explain *all* of the observed dissociation dynamics, it may be possible that N–O bond fission [channel (I)] occurs on an excited state surface, while rearrangement and elimination of NO [channel (II)] is statistically favored on the ground state surface and dominates C–N bond fission [channel (III)] once on that surface. This requires that the RRKM rate constant for NO elimination at a reasonable barrier height be substantially larger than that for C–N bond fission. We have performed RRKM calculations[45] for the two channels to test if this is plausible.

The RRKM rate constants $k(E)$ are given by

$$k(E) = \frac{W^\dagger(E)}{h\rho(E)}. \tag{10}$$

Here, $W^\dagger(E)$ is the sum of internal states of the dissociating complex at the transition state and $\rho(E)$ is the density of states of the reactant. In our calculation, all vibrations were assumed to be separable harmonic oscillators. The rotational temperature was estimated to be 50 K, consistent with previous experiments using this apparatus,[6–9] and the overall rotations were treated adiabatically. Vibrational frequencies for the tight three-center transition state in NO elimination were chosen to yield a preexponential $\log_{10} A$ factor in the Arrhenius rate expression of 13 based on comparisons to previously determined values for comparable types of unimolecular decompositions.[43,46] The vibrational frequencies in the transition state for C–N bond fis-

sion were chosen to be consistent with a $\log_{10} A$ factor of 15.6, determined by Benson and O'Neal from the analysis of kinetics data.[47]

We find that even for a barrier as low as 10 kcal/mol with respect to CH_2NO_2, NO elimination is only four times as fast as C–N bond fission at $\lambda_{diss}=240$ nm. This is the dissociation wavelength where our signal-to-noise ratio is best, and we would definitely observe C–N fission were it occurring to this extent. Moreover, a 10 kcal/mol barrier is not consistent with the translational energy distribution for the NO elimination channel. This distribution peaks around 60 kcal/mol (see Fig. 5), indicating that the barrier with respect to the products is at least this high. Since NO elimination from CH_2NO_2 is exothermic by 33 kcal/mol, the barrier height with respect to CH_2NO_2 must be at least 30 kcal/mol. For this barrier height, statistical C–N bond fission on the ground state surface is faster than NO elimination at 240 nm. Judging by the observed $P(E_T)$ distribution for this channel, the true barrier height is probably larger than this. A barrier of 30 kcal/mol with respect to CH_2NO_2 implies that the potential energy at the barrier must be very efficiently channeled into product kinetic energy, and this is unlikely considering how strained the transition state must be with respect to the products. Our calculations therefore imply that in the statistical limit, elimination of NO cannot be the dominant dissociation channel on the ground state. While there is considerable leeway in some of the assumptions made in our analysis, this conclusion seems quite secure.

2. $CH_2NO_2 \rightarrow H_2CO + NO$ dissociation mechanism

We are left with two options regarding channel (II). Either it proceeds on a ground state surface in a highly nonstatistical (i.e., mode-specific) fashion, or it results from the nuclear dynamics on one or more of the excited state surfaces. Given the considerable molecular rearrangement necessary to produce the observed channel (II) products, in contrast to the very direct C–N simple bond fission channel, the first option seems quite unlikely. This suggests the existence of a mechanism on excited state surfaces that would facilitate dissociation to channel (II) products. After presenting and discussing such a mechanism, we then consider the mechanism for dissociation channel (I), which, based on the above discussion, also most likely occurs on an excited state surface.

Figure 10 depicts the likely nuclear dynamics for the rearrangement-elimination process of channel (II), irrespective of the details of the potential energy surfaces involved. This channel presumably involves (a) rotation of the CH_2 plane perpendicular to the NO_2 plane; (b) O atom transfer through a C–N–O three-membered-ring; and (c) elimination of H_2CO from NO. We note that steps (a) and (b) are the first steps in the mechanism proposed by Yamada and co-workers[48,49] for the photochemical rearrangement of $R'RC{=}NO_2^-$ anions in solution as a synthetic route to the corresponding hydroxamic acids [i.e., RC(O)–N(OH)R]. In their mechanism, as applied to $CH_2NO_2^-$, the anion first undergoes $\pi^* \leftarrow \pi$ excitation corresponding to one electron being transferred from the $2b_1$ HOMO to the $3b_1$ molecular orbital (see Fig. 7). The subsequent dynamics involve CH_2 moiety rotation, which minimizes the C–N antibonding interaction, formation of a three-membered oxaziridine ring as an O atom is transferred from N to C atoms, and finally H atom migration resulting in the observed net isomerization from $CH_2NO_2^-$ to $HC(O)N(O)H^-$. The similarities between the observed rearrangement-elimination products in the neutral CH_2NO_2 radical and the postulated $CH_2NO_2^-$ anion rearrangement dynamics are compelling. Not only are the nuclear motions in the initial two stages of the anion rearrangement mechanism very similar to what must occur in the rearrangement-elimination channel observed with nitromethyl radical, but the initial electronic transition is proposed to be the same in each case (as discussed in Sec. IV B).

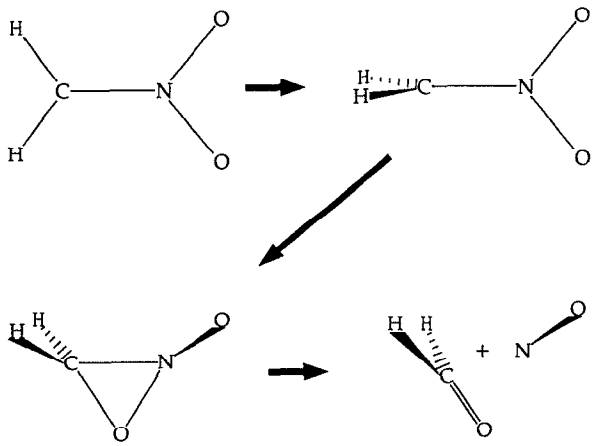

FIG. 10. Nuclear dynamics presumably involved in a channel (II) rearrangement-elimination mechanism resulting in the reaction $CH_2NO_2 \rightarrow H_2CO + NO$.

Although the anion has an additional $2b_1$ electron in both the ground and excited states, one expects the $1\,^2B_1$ state in the radical to be significantly stabilized by a 90° internal rotation about the C–N bond for the same reason as in the anion — reduction of the C–N antibonding interaction as a result of the half-filled $3b_1$ orbital. The resulting stabilization may be greater in the radical because there is no half-filled C–N π-bonding orbital as there is in the anion excited state, or it might be smaller due to the larger C–N bond distance in the radical. In any case, let us consider what effect the 90° internal rotation might have on the relevant molecular orbitals in the excited state. Figure 11(a) shows the $3b_1$ molecular orbital after the internal rotation has occurred. While this orbital has some amplitude on the C atom in the planar geometry, it becomes an orbital localized on the NO_2 group in the 90° geometry, leaving the p orbital on the C atom perpendicular to the CH_2 plane empty. This geometry places an excess positive charge on the C atom and corresponding excess negative charge on the NO_2 moiety. This should facilitate formation of the three-member C–N–O ring intermediate, since the lone pair on either of the oxygen atoms in the NO_2 plane [see Fig. 11(b)] will be attracted to the empty orbital on

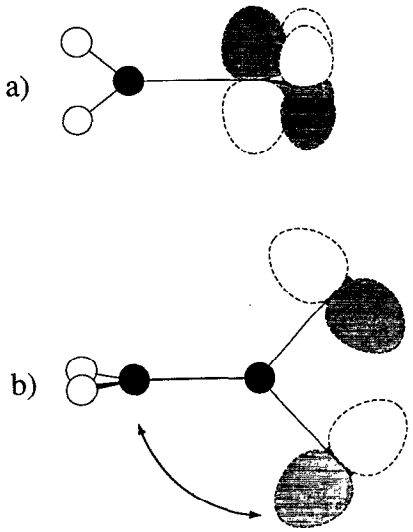

FIG. 11. (a) The form of the $3b_1$ molecular orbital following a 90° internal rotation. (b) A top view of CH_2NO_2 subsequent to internal rotation, showing how a C–O bond may form from attack by the $5b_2$ O atom lone pair molecular orbital at the empty p orbital on the carbon atom.

the electron-poor C atom, forming an O–C bond. Figure 11 may be somewhat of a simplification in that rehybridization of the N atom may occur subsequent to internal rotation, resulting in an sp^3 hybridization with a lone pair of electrons localized on the nitrogen, but this does not affect the overall argument.

As far as the energies along the rather complex reaction coordinate associated with the nuclear dynamics depicted in Fig. 10 are concerned, we expect the highest energy geometry to occur either en route to formation of the three-member ring, or at the three-member ring itself. While one might wonder if the three-member oxaziridine ring represents a local minimum, prior theoretical studies[49] suggest that the structurally identical intermediate postulated for $CH_2NO_2^-$ rearrangement is unstable. In addition, only oxaziridines having aryl-, alkyl-, H-, or acyl-substituted N atoms have been isolated; no stable oxaziridines with O-substituted N atoms (i.e., the current case) are known.[50] In any case, regardless of the exact location of the barrier along the reaction coordinate, we expect it to lie well above ground state H_2CO+NO products, consistent with the high translational energy seen for this channel. On the other hand, the geometry found at the barrier is only beginning to resemble the products, and as a result, there should be extensive internal excitation found in the products. This implies that the actual barrier height with respect to the products is significantly higher than the minimum value of ~60 kcal/mol implied by the translational energy distribution.

The central element in the above mechanism is that the coordinatively unsaturated C atom provides a relatively facile pathway for NO elimination. Such a pathway does not exist in CH_3NO_2, consistent with the absence of NO production as a result of electronic excitation. Moreover, other examples of dissociation channels analogous to channel (II) in our study have been observed in which the C atom in the parent molecule is unsaturated. For example, in the experiments of Beijersbergen *et al.*,[26] three structural isomers of nitromethane radical cation and their deuterated analogs were neutralized by resonant charge exchange. This process forms the neutral with a significant amount of excitation (5.9 eV for Na and 7.2 eV for Cs charge exchange). Below are the structures of two of the isomers studied, nitromethane 1 and its tautomer, *aci*-nitromethane 2.

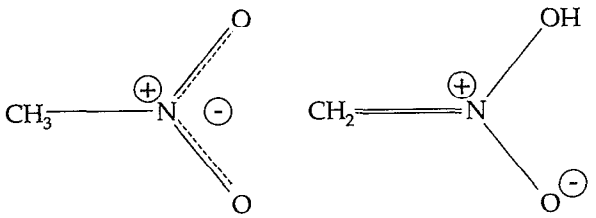

1 2

Rearrangement followed by elimination of NOH (or HNO) was found to be the major pathway only upon charge exchange neutralization yielding the *aci* form of nitromethane, which contains a CH_2 group rather than a CH_3 group bonded to the nitrogen atom. Also, in the recent study by Galloway *et al.*[51] of the UV photodissociation of nitrobenzene, NO elimination was observed, along with both C–N and N–O bond fission. While nitrobenzene is a closed shell molecule, the C atom bound to the NO_2 group is coordinatively unsaturated, and this may enhance the NO elimination channel by the mechanism discussed above.

3. $CH_2NO_2 \rightarrow CH_2NO+O$ dissociation mechanism

Having proposed a possible mechanism by which channel (II) proceeds to products, the next step is to determine whether the absence of C–N bond fission and the presence of N–O fission can also be explained in terms of excited state dynamics. We first consider why C–N fission might not readily occur from the initially accessed $1\,^2B_1$ state. As shown in Fig. 8, the three lowest lying C–N bond fission channels which could correlate to this state in C_{2v} symmetry are (IIIa) $CH_2(\tilde{X}\,^3B_1)+NO_2(\tilde{X}\,^2A_1)$; (IIIb) $CH_2(\tilde{b}\,^1B_1)+NO_2(\tilde{X}\,^2A_1)$; and (IIIc) $CH_2(\tilde{a}\,^1A_1)+NO_2(1\,^2B_1)$. The observed absence of C–N bond fission in our results requires that there is no low energy pathway for dissociation of this state to the ground state fragments [channel (IIIa)]. If we examine how the molecular orbitals of the parent molecule correlate with those of the fragments, we indeed find that the ground state fragments correlate diabatically (and adiabatically) with the $\tilde{X}\,^2B_1$ state of CH_2NO_2 and not with the $1\,^2B_1$ state. Hence, channel (IIIc) is the lowest C–N bond fission channel to which the $1\,^2B_1$ state can correlate diabatically. This channel lies 45 kcal/mol above the lowest CH_2NO+O channel. C–N bond fission is therefore less favorable than might be ex-

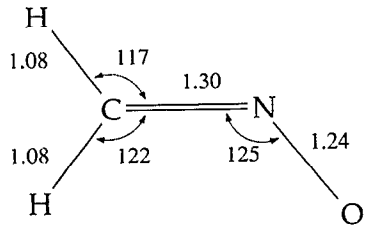

FIG. 12. Geometry of ground state CH_2NO, as determined in Ref. 52.

pected at first glance, and any additional barrier along the reaction coordinate further reduces the expected contribution from this channel.

To complete the overall picture, we need to identify a facile dissociation pathway to N–O bond fission consistent with the observed translational energy distribution. This distribution, which at 240 nm peaks at less than 15% of the available kinetic energy, indicates that the surface on which dissociation occurs is not strongly repulsive along the N–O coordinate. We first consider which electronic states of CH_2NO_2 might lead to CH_2NO+O production. The geometry of the ground state of CH_2NO calculated by Balakina *et al.*[52] is shown in Fig. 12. This radical has C=N double bond character, while the HOMO of the $1\,^2B_1$ state of CH_2NO_2 (the $3b_1$ molecular orbital) is C–N π antibonding. Hence, the $1\,^2B_1$ state should not diabatically correlate to the ground state of CH_2NO. On the other hand, the $1\,^2A_2$ state has a C–N double bond and lies well below the CH_2NO+O asymptote. Moreover, the C–N double bond makes dissociation to CH_2+NO_2 unlikely. Dissociation to CH_2NO+O from the $1\,^2A_2$ state therefore presents an attractive possibility.

The next issue to address is the mechanism which allows the radical to transfer onto the $1\,^2A_2$ surface after initial excitation to the $1\,^2B_1$ state. The molecular orbital occupancies for these states in the planar geometry, $\cdots(1a_2)(2b_1)^2$ for the former and $\cdots(1a_2)^2(3b_1)$ for the latter, differ by two electrons and are therefore coupled only by the configuration interaction term in the electronic Hamiltonian. This coupling should be strong only in the vicinity of an intersection between the two surfaces; such an intersection can be brought about by internal rotation about the C–N bond. As discussed above, this torsional motion is expected to stabilize the initially excited $1\,^2B_1$ state. In contrast, it should strongly destabilize the $1\,^2A_2$ state as it disrupts the C–N double bond in the planar geometry. One can therefore imagine a crossing between the two surfaces at an internal rotation angle between 0° and 90°, as shown in Fig. 13. The radical has no symmetry at the intermediate angles, so these would actually be avoided crossings, with the adiabatic surfaces repelling each other near where the intersections would occur in the absence of configuration interaction. It is perhaps easier to think about the overall dynamics in terms of diabatic surfaces. If, at the crossing points, the radical remains on the initial diabatic surface, it will continue to undergo internal rotation until it reaches the 90° geometry, at which point NO elimination is most favorable. On the other hand, it

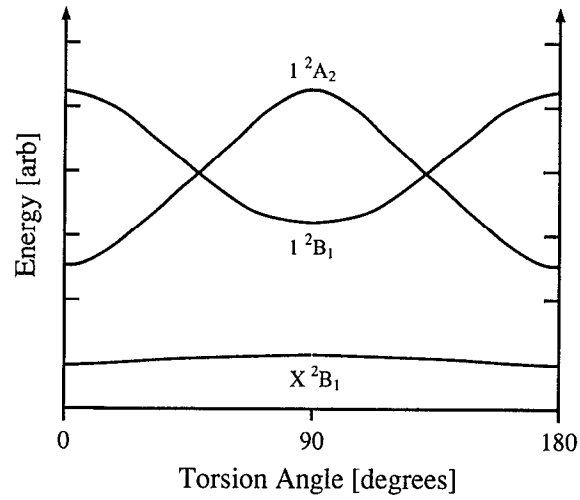

FIG. 13. A schematic of the potentials for the $1\,^2B_1$ state and $1\,^2A_2$ state along the torsion coordinate.

can undergo a transition to the diabatic surface which correlates to the $1\,^2A_2$ state in the planar geometry. Such a diabatic transition would most likely result in a highly vibrationally excited molecule. If we apply the concepts developed for statistical dissociation on ground state surfaces to this situation, we would expect that dissociation to fragments with high kinetic energy is unlikely because the $1\,^2A_2$ state is strongly bound with respect to CH_2NO+O. This is consistent with our observed distribution. However, a translational energy distribution described by phase space theory would peak very close to zero, while ours actually peaks at 5–8 kcal/mol. This may indicate a small barrier to N–O bond fission. Alternatively, peaking away from zero may indicate that the dissociation rate is sufficiently rapid as to render the statistical perspective somewhat inappropriate.

Overall, the picture we are proposing to explain the photodissociation of CH_2NO_2 is that the important nuclear dynamics are occurring on excited state potential energy surfaces. In particular, torsional motion on the initially excited surface plays a major role in the two observed dissociation channels, and the outcome depends on whether a diabatic transition occurs while the radical is undergoing internal rotation. We acknowledge that aspects of these mechanisms are somewhat speculative. Nonetheless, as the overall scheme is consistent with the experimental results, it should at least provide a starting point for more detailed experimental and theoretical studies of this species. We believe that *ab initio* investigations of the excited states of CH_2NO_2 would be particularly helpful in assessing some of the ideas put forward here.

V. CONCLUSIONS

We have studied the photodissociation dynamics of the CH_2NO_2 radical at three wavelengths 240, 255, and 270 nm. We have measured branching ratios for the various dissociation channels, as well as kinetic energy and angular distributions for each major channel. We observe only two

channels and find these have comparable yields (I) $CH_2NO_2 \rightarrow CH_2NO_2 + O$ and (II) $CH_2NO_2 \rightarrow H_2CO + NO$. No C–N bond fission is observed. These results are in sharp contrast to the ultraviolet photodissociation of nitromethane, which undergoes exclusive C–N bond fission near 200 nm. We have assigned the electronic transition in these experiments to the $1\,^2B_1 \leftarrow \tilde{X}\,^2B_1$ transition, in which the $2b_1$ C–N π-bonding electron is promoted to the $3b_1$ π^* molecular orbital. An analysis of the observed branching ratios and translational energy distributions indicates that statistical dissociation on the ground state surface is most likely not occurring, and that both of the observed channels are occurring on excited state surfaces. Mechanisms for both channels are proposed in which the initial nuclear dynamics involves internal rotation about the C–N bond in the initially excited state. A 90° internal rotation facilitates formation of the three-center C–N–O transition state needed for NO elimination, while internal rotation also provides a reasonable coupling mechanism between the $1\,^2B_1$ and lower-lying $1\,^2A_2$ surface, with N–O bond fission occurring on the latter surface.

ACKNOWLEDGMENTS

This research is supported by the Director, Office of Basic Energy Sciences, Chemical Sciences Division of the U. S. Department of Energy under Contract No. DE-AC03-76SF00098. Additional support is provided by the National Science Foundation under Grant No. CHE91-08145. The authors acknowledge the contributions of Dr. Ricardo B. Metz in the acquisition of preliminary data. We thank Dr. Carl Melius for access to data prior to publication and Dr. Sean Smith for useful discussions.

[1] *Molecular Photodissociation Dynamics*, edited by M. N. R. Ashfold and J. E. Baggott (Royal Society of London, London, 1987).
[2] G. E. Busch, J. F. Cornelius, R. T. Mahoney, R. I. Morse, D. W. Schlosser, and K. R. Wilson, Rev. Sci. Instrum. **41**, 1066 (1970); G. E. Busch and K. R. Wilson, J. Chem. Phys. **56**, 3626 (1972).
[3] For a recent review, see M. N. R. Ashfold, I. R. Lambert, D. H. Mordaunt, G. P. Morley, and C. M. Western, J. Phys. Chem. **96**, 2938 (1992).
[4] E. J. Hintsa, X. Zhao, W. M. Jackson, W. B. Miller, A. M. Wodtke, and Y. T. Lee, J. Phys. Chem. **95**, 2799 (1991).
[5] H. F. Davis, B. Kim, H. S. Johnston, and Y. T. Lee, J. Phys. Chem. **97**, 2172 (1993).
[6] R. E. Continetti, D. R. Cyr, R. B. Metz, and D. M. Neumark, Chem. Phys. Lett. **182**, 406 (1991).
[7] D. R. Cyr, R. E. Continetti, R. B. Metz, D. L. Osborn, and D. M. Neumark, J. Chem. Phys. **97**, 4937 (1992).
[8] R. E. Continetti, D. R. Cyr, D. L. Osborn, D. J. Leahy, and D. M. Neumark, J. Chem. Phys. **99**, 2616 (1993).
[9] D. J. Leahy, D. R. Cyr, D. L. Osborn, and D. M. Neumark, Chem. Phys. Lett. (in press).
[10] L. F. Salter and B. A. Thrush, J. Chem. Soc., Faraday Trans. I **37**, 2025 (1977).
[11] M. E. Jacox, J. Phys. Chem. **87**, 3126 (1983).
[12] C. Chachaty, J. Chim. Phys. **62**, 728 (1965).
[13] C. Chachaty and C. Rosilio, J. Chim. Phys. **64**, 777 (1967).
[14] M. E. Jacox, J. Phys. Chem. **91**, 5038 (1987).
[15] R. B. Metz, D. R. Cyr, and D. M. Neumark, J. Phys. Chem. **95**, 2900 (1991).
[16] M. L. McKee, J. Am. Chem. Soc. **107**, 1900 (1985).
[17] M. L. McKee, J. Chem. Phys. **81**, 3580 (1984).
[18] L. J. Butler, D. Krajnovich, Y. T. Lee, G. Ondrey, and R. Bersohn, J. Chem. Phys. **79**, 1708 (1983).
[19] N. C. Blais, J. Chem. Phys. **79**, 1723 (1983).
[20] K. Q. Lao, E. Jensen, P. W. Kash, and L. J. Butler, J. Chem. Phys. **93**, 3958 (1990).
[21] D. B. Moss, K. A. Trentelman, and P. L. Houston, J. Chem. Phys. **96**, 237 (1991).
[22] D. L. Phillips and A. B. Myers, J. Phys. Chem. **95**, 7164 (1991).
[23] P. E. Schoen, M. J. Marrone, J. M. Schnur, and L. S. Goldberg, Chem. Phys. Lett. **90**, 272 (1982).
[24] A. M. Wodtke, E. J. Hintsa, and Y. T. Lee, J. Chem. Phys. **84**, 1044 (1986).
[25] A. M. Wodtke, E. J. Hintsa, and Y. T. Lee, J. Phys. Chem. **90**, 3549 (1986).
[26] J. H. M. Beijersbergen, W. J. van der Zande, P. G. Kistemaker, J. Los, T. Drewello, and N. M. M. Nibbering, J. Phys. Chem. **96**, 9288 (1992).
[27] D. J. Leahy, D. R. Cyr, D. L. Osborn, and D. M. Neumark, SPIE Proc. **1858**, 49 (1993).
[28] M. A. Johnson, M. L. Alexander, and W. C. Lineberger, Chem. Phys. Lett. **112**, 285 (1984).
[29] R. E. Continetti, D. R. Cyr, and D. M. Neumark, Rev. Sci. Instrum. **63**, 1840 (1992).
[30] J. M. B. Bakker, J. Phys. E **6**, 785 (1973); **7**, 364 (1974).
[31] D. P. de Bruijn and J. Los, Rev. Sci. Instrum. **53**, 1020 (1982).
[32] C. Martin, P. Jelinsky, M. Lampton, R. F. Malina, and H. O. Anger, Rev. Sci. Instrum. **52**, 1067 (1981).
[33] D. F. Ogletree, G. S. Blackman, R. Q. Hwang, U. Stark, G. A. Somorjai, and J. E. Katz, Rev. Sci. Instrum. **63**, 104 (1992).
[34] S. G. Lias, J. E. Bartmess, J. F. Liebman, J. L. Holmes, R. D. Levin, and W. G. Mallard, J. Phys. Chem. Ref. Data. **17**, Suppl. 1 (1988).
[35] R. N. Zare, Mol. Photochem. **4**, 1 (1972).
[36] C. F. Melius (private communication).
[37] P. Ho, D. J. Bamford, R. J. Buss, Y. T. Lee, and C. B. Moore, J. Chem. Phys. **76**, 3630 (1982).
[38] R. P. Saxon and M. Yoshimine, Can. J. Chem. **70**, 572 (1992).
[39] A. P. Cox and S. Waring, J. Chem. Soc. Faraday Trans. **2**, 1060 (1972).
[40] M. J. Frisch, M. Head-Gordon, H. B. Schlegel, K. Raghavachari, J. S. Binkley, C. Gonzalez, D. J. DeFrees, D. J. Fox, R. A. Whiteside, R. Seeger, C. F. Melius, J. Baker, R. L. Martin, L. R. Kahn, J. J. P. Stewart, E. M. Fluder, S. Topiol, and J. A. Pople, Gaussian Inc. Pittsburgh, PA.
[41] F. T. Williams, Jr., P. W. K. Flanagan, W. J. Taylor, and H. Schechter, J. Org. Chem. **30**, 2674 (1965).
[42] For general reviews of RRKM theory, see W. Forst, J. Chim. Phys. **87**, 715 (1990); *Theory of Unimolecular Reactions* (Academic, New York, 1973); P. J. Robinson and K. A. Holbrook, *Unimolecular Reactions* (Wiley-Interscience, New York, 1972).
[43] R. G. Gilbert and S. C. Smith, *Theory of Unimolecular and Recombination Reactions* (Blackwell, Oxford, 1990).
[44] "Loose" and "tight" relate to the relative gain in entropy on going from the equilibrium geometry to the activated complex, with "loose" implying a larger gain and vice-versa.
[45] D. L. Bunker and W. L. Hase, Quantum Chemistry Program Exchange catalog number QCPE-234, Department of Chemistry, Indiana University.
[46] S. W. Benson, *Thermochemical Kinetics*, 2nd ed. (Wiley, New York, 1976).
[47] S. W. Benson and H. E. O'Neal, Natl. Stand. Ref. Data Ser., Natl. Bur. of Stand. **21**, 473 (1970).
[48] K. Yamada, T. Kanekiyo, S. Tanaka, K. Naruchi, and M. Yamamoto, J. Am. Chem. Soc. **103**, 7003 (1981).
[49] O. Kikuchi, T. Kanekiyo, S. Tanaka, K. Naruchi, and K. Yamada, Bull. Chem. Soc. Jpn. **55**, 1509 (1982).
[50] E. Schmitz, *Comprehensive Heterocyclic Chemistry*, edited by W. Lwowski (Pergamon, Oxford, 1984).
[51] D. B. Galloway, J. A. Bartz, L. G. Huey, and F. F. Crim, J. Chem. Phys. **98**, 2107 (1993).
[52] M. Y. Balakina, M. B. Zuev, and I. D. Morozova, J. Mol. Struct. (Theochem.) **183**, 291 (1989).